JGR Solid Earth

RESEARCH ARTICLE
10.1029/2019JB018788

Deformation of Intrasalt Beds Recorded by Magnetic Fabrics

R. Issachar[1], R. Weinberger[1,2], G. I. Alsop[3], and T. Levi[1]

[1]Geological Survey of Israel, Jerusalem, Israel, [2]Department of Geological and Environmental Sciences, Ben Gurion University of the Negev, Beer Sheva, Israel, [3]Department of Geology and Geophysics, School of Geosciences, University of Aberdeen, Aberdeen, UK

Key Points:
- Magnetic fabrics are used to study the deformation and kinematics of thick intrasalt beds within the Sedom salt wall in the Dead Sea Basin
- Magnetic fabrics show tectonic imprints due to folding associated with passive diapirism
- Thick intrasalt beds are mechanically distinct from the flowing salt and preserve information on salt tectonic processes operating at depth

Correspondence to:
R. Issachar,
ranissachar@gmail.com

Citation:
Issachar, R., Weinberger, R., Alsop, G. I., & Levi, T. (2019). Deformation of intrasalt beds recorded by magnetic fabrics. *Journal of Geophysical Research: Solid Earth*, *124*, 12,465–12,483. https://doi.org/10.1029/2019JB018788

Received 27 SEP 2019
Accepted 23 NOV 2019
Accepted article online 28 NOV 2019
Published online 23 DEC 2019

Abstract Intrasalt beds comprise sedimentary layers within a weak rock salt mass. Thick intrasalt beds (hundred meter scale) are common in salt structures, yet their internal deformation has not been investigated in detail as outcrops of such beds are rare. In this study, we explore the internal deformation of thick intrasalt beds exposed along the Sedom salt wall in the Dead Sea Basin. These beds are highly deformed and form a kilometer-scale recumbent fold. We measured the magnetic fabrics from six sites along these beds. Magnetic fabrics reflect the preferred alignment of crystals and grain shapes and are a proven kinematic marker in deformed rocks. Our analysis shows that the magnetic fabrics are mostly controlled by the preferred orientation of clay minerals. The orientations of the principal susceptibility axes vary along the salt wall regardless of the specific rock type. Minimum susceptibility axes (K_3 axes) are normal to bedding, whereas maximum susceptibility axes (K_1 axes) are subparallel to bedding strike. We suggest that the magnetic fabrics were acquired by strain imposed at a necked region along a subsurface fault, together with folding during passive diapirism. Generally, the magnetic fabrics have not been influenced by the later stage of active diapirism, which led to emergent beds at the surface. Nevertheless, in sites from the upper limb of the recumbent fold, the magnetic fabrics were further deformed by folding at the base of a salt glacier. Our results demonstrate that thick intrasalt beds are mechanically distinct from the encasing flowing salt and preserve information on salt tectonic processes operating at depth.

Plain Language Summary Salt structures are generally associated with large amounts of deformation. We studied the deformation of thick intrasalt beds within the exposed Sedom salt wall in the Dead Sea Basin. Due to the solubility of rock salt, exposures of salt structures are very rare and, therefore, the Sedom salt wall offers a unique opportunity to study outcrops of thick intrasalt beds. These beds comprise thick sedimentary layers (~200 m) that are surrounded by rock salt. We investigate the microstructural deformation of the rocks by measuring the magnetic fabrics of samples from six sites in the intrasalt beds along the salt wall. Magnetic fabrics provide a kinematic marker, as they usually reflect the preferred alignment of crystals and grain shapes within a rock sample. We found that the thick intrasalt beds record deformation that was acquired in the subsurface at a necked region, when the beds were folded from horizontal to subvertical attitudes along a subsurface fault. At a later stages of vertical flow along the salt wall, which led to emergent beds at the surface, no internal deformation was developed. This study demonstrates that thick intrasalt beds are mechanically distinct from the encasing flowing salt and thereby preserve information on salt tectonic processes operating at depth.

1. Introduction

The rheological properties of salt enable it to flow under gravitational and lateral tectonic forces, thereby forming large-scale salt structures (Jackson & Hudec, 2017; Urai et al., 2008). The internal deformation within salt structures is important to gain a better understanding of the kinematics and mechanics of salt flow and is critical when using salt bodies as potential waste repositories and hydrocarbon targets (e.g., Archer et al., 2012; Jackson & Hudec, 2017; Warren, 2016, 2017). Intrasalt beds are relatively competent layers of evaporite deposits (anhydrite and gypsum), clastic rocks (shales and siliciclasts) or carbonate rocks which are embedded within the weak rock salt mass (Warren, 2016). They are used as kinematic markers to study the internal deformation within salt structures (Rowan et al., 2019). Because intrasalt beds are relatively strong compared to the weak encasing rock salt, they form a wide variety of structures across a range of scales (Jackson & Hudec, 2017). Studies of intrasalt beds are usually reliant on salt mine surveys (e.g.,

Burliga, 2018), seismic interpretations (e.g., Jackson et al., 2014), analog models (e.g., Koyi, 2001; e.g., Dooley et al., 2015), numerical modeling (e.g., Li et al., 2012), and observations from outcrops (e.g., Alsop et al., 2015; Davison et al., 1996); although the latter are limited due to the paucity of salt exposures.

In this study, we investigate the deformation of thick (~200 m) intrasalt beds exposed within an elongated ridge of diapiric salt that forms a salt wall (Jackson & Hudec, 2017). We use the unique opportunity offered by the Sedom salt wall in which both rock salt and thick intrasalt beds are exposed and accessible for sampling along the western side of the Dead Sea Basin (Figure 1). Studies of thin (millimeter to decimeter scale) intrasalt beds from salt mines in Spain and Poland (Burliga, 2014, 2018; Sans et al., 1996) and from outcrops in Iran and Israel (Alsop et al., 2015; Talbot, 1998) show that the thin intrasalt beds preserve details of folding and thrusting due to salt flow. The deformation of thick (meter to hundred-meter scale) intrasalt beds is mostly studied from high-resolution seismic data. These data provide a description of the large-scale geometries but cannot image the details of intrasalt beds (Jackson & Hudec, 2017). Three-dimensional seismic data from NW Europe (Van Gent et al., 2011) and offshore Brazil (Fiduk & Rowan, 2012; Jackson et al., 2014) show complex geometries of folds and boudins, which only partly reflect the overall geometry of the surrounding salt structures. These data demonstrate that thick intrasalt beds commonly form independent mechanical units within the salt bodies (Rowan et al., 2019). Numerical models demonstrate the sensitivity of thick intrasalt beds to geometrical and mechanical variables, such as the initial position and thickness of the beds, and the viscosity of the encasing rock salt (Chemia & Koyi, 2008; Li, 2016; Li et al., 2012). Moreover, conceptual models founded on natural observations and analog and numerical models suggest that the style and extent of deformation of thick intrasalt beds varies significantly for different modes of salt tectonics, that is, passive or active diapirism (Rowan et al., 2019).

In order to shed light on the internal deformation of salt walls and the role played by intrasalt beds, we investigated ~200-m-thick clastic beds that are embedded within 2,000 m of rock salt that form the Sedom salt wall in the Dead Sea Basin. The Sedom salt wall is one of the few places on Earth where thick intrasalt beds and adjacent salt are exposed at the surface. The large-scale setting of these beds was previously determined by means of field mapping (Zak, 1967), stratigraphy (Zak et al., 1968), paleomagnetism (Weinberger et al., 1995, 1997), and mesoscale analysis (Alsop et al., 2015, 2018). In this study, we provide further insights from the results of magnetic fabric analysis, which was recently shown to be a promising tool for assessing deformation within exposed salt bodies (Santolaria et al., 2015; Soto et al., 2014) (see section 3.2).

2. The Sedom Salt Wall

The Sedom salt wall is located along the segmented Dead Sea Fault (DSF) system, a continental transform boundary between the African (Sinai) and Arabian plates (Figure 1a). Several elongate depressions are located along the DSF, reflecting local transtension (Garfunkel, 1981). The Dead Sea Basin is approximately 150-km-long, 16-km-wide, 12-km-deep rhomb-shaped, pull-apart graben that formed between longitudinal left-stepping sinistral faults (Garfunkel, 2014). The basin is bound by the ~N-S trending Eastern and Western Border Faults (Figure 1a). In its southwestern margin, a set of longitudinal subsurface normal faults, including the prominent Sedom Fault, separates the intermediate block to the west from the deep block to the east (Larsen et al., 2002; Figure 1b). The transverse Amazyahu Fault bounds the basin on the southern side (Figure 1a). The basin fill comprises Neogene siliciclastics (Hazeva Formation), evaporites (Sedom Formation), and postevaporitic lacustrine and fluvial sediments (Amora and Lisan formations) (Kashai & Crocker, 1987). The top of the evaporate series is found at depths of ~5 km in the deep block and at ~2 km in the intermediate block (Figure 1b) (Kashai & Crocker, 1987). The southern basin hosts two main salt structures, the exposed Sedom salt wall, and the subsurface Lisan diapir further to the north (Figure 1a). Estimates suggest that the Sedom salt wall has an overall volume of ~60 km^3, which is significantly less than the ~780 km^3 of the unexposed Lisan diapir (Al-Zoubi & ten Brink, 2001). The evaporite series known as the Sedom Formation outcrops along the Sedom salt wall and is divided into five members (Zak, 1967) (Figure 2), several of which are thick (100–200 m) intrasalt siliciclastic-carbonate beds. The oldest Karbolet salt and shale member has an overall thickness >550 m and consists of alternating layers of rock salt (halite), mudstone, sandstone, and dolostone. The Lot salt member has an overall thickness of 700–1,000 m and consists of rock salt (halite) with fine anhydrite and gypsum layers. The Bnot Lot shale member, which has an overall thickness of 150–170 m, is comprised of beds of dolostone, mudstone, clay, sandstone, gypsum, and anhydrite. The

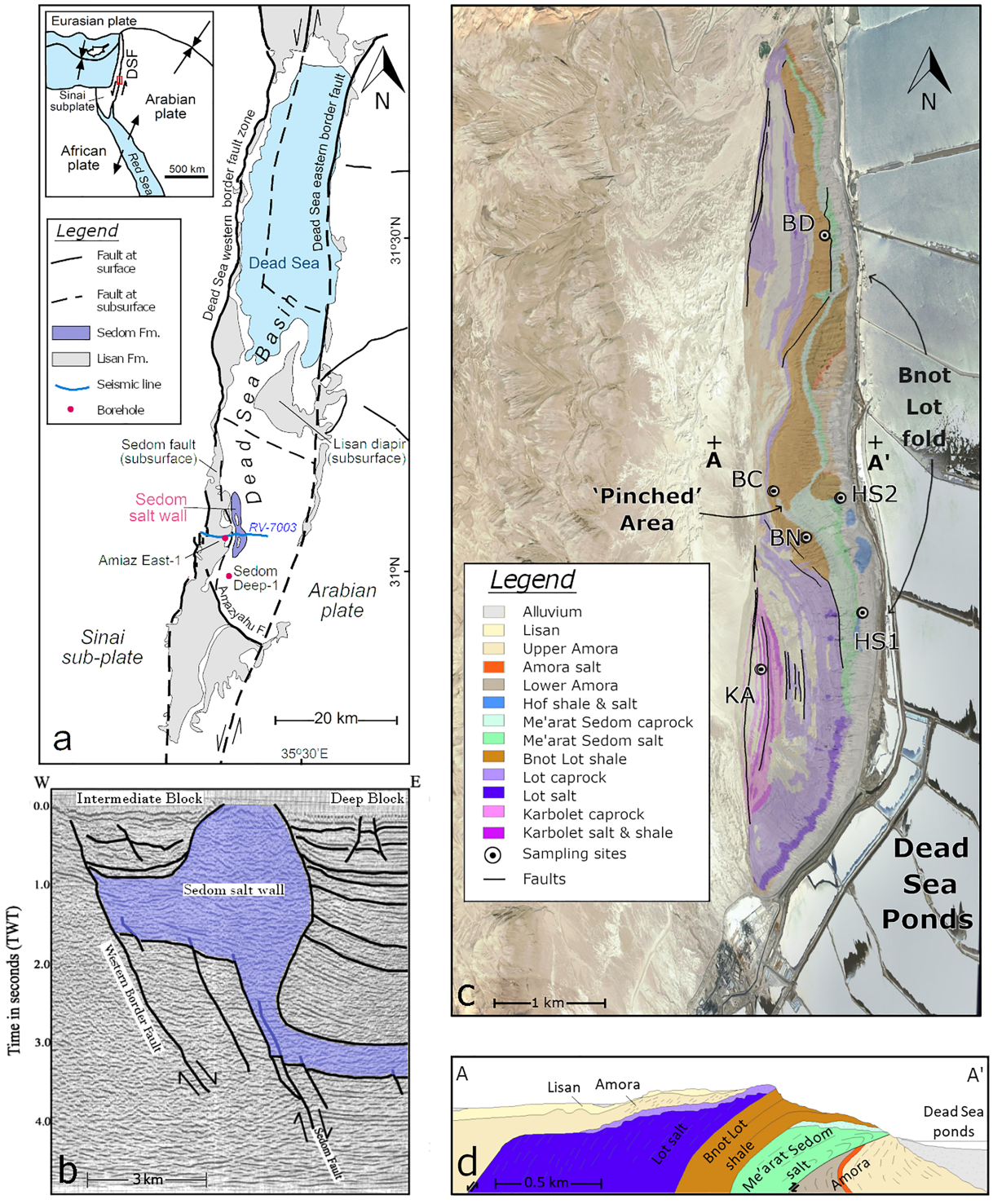

Figure 1. (a) Tectonic setting of the Dead Sea Fault (DSF) area. Red box marks the study area at the Dead Sea Basin. The exposed Sedom salt wall is shown, with fault traces are from Sneh and Weinberger (2014). Solid blue line marks the location of the seismic line in (b). Names of faults are indicated. (b) Two-way-travel time (TWT) seismic line RV-7003 across the Sedom salt wall showing the Western Border Fault and the Dead Sea Basin structural blocks (from Larsen et al., 2002). (c) Detailed geological map of Mount Sedom (after Agnon et al., 2006) draped on a Google Earth image. Sampling sites are marked with circles. A major recumbent fold termed Bnot Lot fold is marked. Location of cross section in (d) is indicated by A-A′. (d) West-east cross section through the central part of the Sedom salt wall (after Zak, 1967).

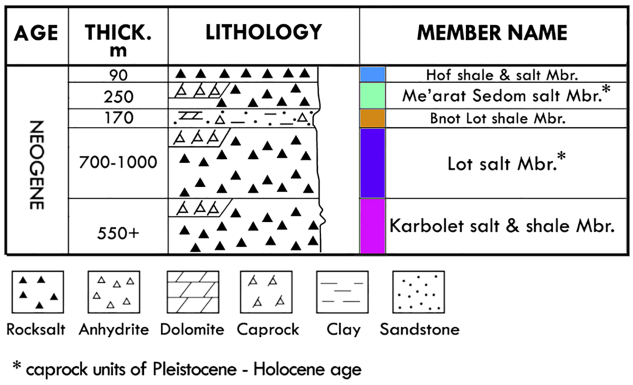

Figure 2. General stratigraphy of the Sedom Formation (after Agnon et al., 2006).

Me'arat Sedom salt member has an overall thickness of 200–250 m and consists of massive rock salt (halite) layers with fine anhydrite and gypsum layers. The Hof shale and salt member has an overall thickness of ~90 m and consists of beds of sandstone, clay, rock salt, and anhydrite. The Sedom salt wall is capped by a ~40-m-thick insoluble layer (caprock), which formed during dissolution of the various salt members and has a flat dissolution surface underneath often termed a "salt mirror" (Zak, 1967; Zucker et al., 2019).

The Sedom salt wall forms a ~10-km-long and 2-km-wide, north-south trending topographical ridge that rises ~240 m above the level of the Dead Sea ponds (currently 410 m below sea level) and contains a central "pinched" ("hour glass") section (Figure 1c). The northeastern side of the ridge is marked by a major recumbent fold, termed the Bnot Lot fold, which can be traced for 5 km along bedding strike to the north of the "pinched" central section of the Sedom salt wall (Figures 1d and 3). The fold is characterized by a steep (60–80°) northeast dipping lower limb and a gently west dipping upper limb that can be traced for 500 m across strike toward the east (Alsop et al., 2015). The upper limb is overturned and underwent >90° and up to 200° of rotation since deposition of the beds (Weinberger et al., 1995, 1997). The southern part of the ridge has the form of an antiform, which was sourced from two adjoining but different basins, the deep block to the east and the intermediate block to the west (Frumkin, 1996; Weinberger et al., 1997).

The occurrence of the thick evaporite sequence of the Sedom Formation in the southern Dead Sea Basin indicates that a substantial and rapid subsidence was already occurring in the Miocene (Garfunkel, 2014; Zak, 1967). Al-Zoubi and ten Brink (2001) suggested that the initiation of salt flow was related to rapid subsidence resulting from local extension within the basin. Based on seismic and borehole data, Weinberger et al. (2006) proposed that significant growth of Sedom salt wall occurred after accumulation of ~2,400 m of overburden (Figure 1b). The initial stages of the Sedom salt wall rise are considered mostly passive and marked by rotated unconformities and halokinetic sequences (e.g., Alsop et al., 2016). Nevertheless, active diapirism associated with salt extrusion and breccia horizons, reflecting shedding of sediments off the rising salt wall, is proposed at 420 ka (Alsop et al., 2015, 2016). During the last 70 ka, the Sedom salt wall is considered to have risen mostly by active diapirism. Uplift rates of 5–11 mm/year in the last 14 ka are well documented by the presence of uplifted late-Pleistocene Lisan sediments on top of the ridge (Weinberger et al., 2007), displacement of the "salt mirror" (Zucker et al., 2019), and hanging passages in caves (Frumkin, 1996). The current uplift rates, calculated from interferometric synthetic aperture radar (InSAR), are similar (Weinberger et al., 2006).

3. Methodology

3.1. Sampling

Six sites were sampled from within the intrasalt beds (Figure 1c). For each sampling site, 15 to 20 oriented cores of 25.4-mm diameter were recovered. Site KA comprises siltstone of the Karbolet salt and shale member within the southern parts of the salt wall. Sites BD, BC, and BN are from within the Bnot Lot shale member and are located at different structural domains around the Bnot Lot fold. Site BD comprises red sandstone from the northern part of the salt wall and is located on the overturned upper limb of the Bnot Lot fold. Site BC comprises siltstone from the central part of the salt wall and is also positioned on the overturned upper fold limb. Site BN is located along a small creek in the central part of the salt wall and is positioned on the steep lower fold limb. At this site, a complete section of the Bnot Lot shale member is exposed and accessible for sampling. We sampled six different rock units (10–20 samples in each) along this section, in order to test the possible effect of composition and rock type on magnetic fabrics. The lithologies are (from bottom to top): Unit 1, gray shales; Unit 2, red sandstone; Unit 3, greenish claystone; Unit 4, brownish siltstone; Unit 5, greenish siltstone; and Unit 6, yellow sandstone. Sites HS1 and HS2 consist of gray siltstone and red sandstone, respectively, of the Hof shale and salt member exposed next to the eastern margins of the salt wall.

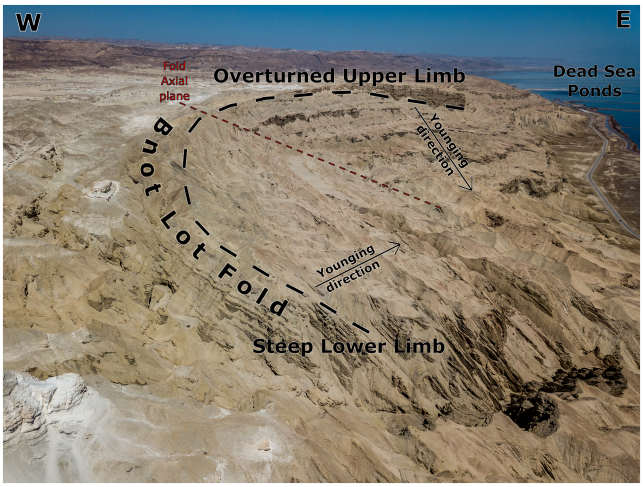

Figure 3. Drone photograph from top of Mount Sedom, showing the kilometer-scale Bnot Lot fold. Arrows indicate sense of younging preserved in the Bnot Lot shales. The red line marks the trace of the axial plane at the surface (after Alsop et al., 2015). The white outcrops are the late-Pleistocene Lisan Formation, which have been uplifted by the rising salt wall (see details in Weinberger et al., 2007). Photography by Iyad Swead.

3.2. Magnetic Fabrics

Magnetic fabrics of rocks evolve by averaging out the orientation-distribution of crystals and grain shapes in a rock specimen and as such provides a powerful petrofabric tool for studying the deformation within intrasalt beds. Magnetic fabrics of sedimentary rocks are used to characterize petrofabrics and weak internal deformation and thus reveal various geological processes such as sedimentation, flow, and tectonic deformation. The magnetic fabric describes the magnetic susceptibility second-rank tensor of a rock sample with eigenvectors (or axes) $\boldsymbol{K_1}$, $\boldsymbol{K_2}$, and $\boldsymbol{K_3}$ (maximum, intermediate, and minimum), which correspond to k_1, k_2, and k_3 eigenvalues. The parameters used to quantify the magnetic fabric are the mean susceptibility ($k_m = k_1 + k_2 + k_3/3$); the degree of anisotropy ($P = k_1/k_3$); and the shape of the anisotropy ($T = 2\ln(k_2/k_3)/\ln(k_1/k_3) - 1$) (e.g., Jelinek, 1981; Borradaile, 2013, p. 291).

The magnetic fabric axes commonly align coaxially with the principal axes of finite strain in different geological conditions. In the depositional environments $\boldsymbol{K_3}$ axes form clusters normal to bedding planes and parallel to the direction of compaction, while $\boldsymbol{K_1}$ and $\boldsymbol{K_2}$ axes are scattered within bedding planes (e.g., Borradaile & Henry, 1997). This kind of fabric is commonly termed a "deposition fabric." During tectonic deformation, all three axes of the magnetic fabric often form clusters (triaxial fabric), with their directions related to the principal strain orientations (Borradaile & Jackson, 2010). This kind of fabric is commonly termed a "tectonic fabric." In weakly tectonically deformed rocks, clusters of $\boldsymbol{K_3}$ axes may remain perpendicular to bedding and clusters of $\boldsymbol{K_1}$ axes are oriented along the intersection of bedding and the tectonic flattening plane (Parés, 2015). In progressive strain regimes, clusters of $\boldsymbol{K_1}$ and $\boldsymbol{K_3}$ axes are oriented parallel to extension and shortening directions, respectively (Borradaile & Jackson, 2010).

Different minerals in rocks may respond to strain in various ways and may also form at different times during the geological history. To correlate the magnetic fabrics with specific crystal and grain orientations and to describe the fabric of different minerals, several experimental techniques are used. The anisotropy of magnetic susceptibility (AMS) is the most common and immediate technique. The magnetization of the sample is measured in various directions under the presence of a low magnetic field (up to 450 A/m). The AMS measured at room temperature is noted as RT-AMS. The AMS measured at low temperature (LT-AMS), usually the boiling temperature of liquid nitrogen, enhances the magnetic fabric of paramagnetic minerals. The anisotropy of anhysteretic remanence magnetization (AARM) describes the magnetic fabric of just the ferromagnetic minerals by measuring magnetization in the absence of a magnetic field, after being magnetized along different directions using a weak direct magnetic field (DC) superimposed on a stronger alternating magnetic field (AC) that decays with time. By using this procedure, the remanence susceptibility tensor is

calculated, as defined by mean remanence susceptibility k_R, eigenvectors $\boldsymbol{K_{R1}}$, $\boldsymbol{K_{R2}}$, and $\boldsymbol{K_{R3}}$ and eigenvalues k_{R1}, k_{R2}, and k_{R3} (Jackson, 1991).

For all sites, we measured RT-AMS, LT-AMS, and AARM. RT-AMS and LT-AMS were measured at a low magnetic field of 450 A/m and a frequency of 976 Hz with a KLY-4S Kappabridge (AGICO Inc.) at the Geological Survey of Israel. LT-AMS was measured according to the procedure presented by Issachar et al. (2016). The samples were cooled in a liquid nitrogen bath for 50 min before the first measurement and for 5 min between axial and mean susceptibility measurements. The Kappabridge coil was protected from the cold sample with a thin silicon sheet, and the samples were wrapped with a Teflon layer to prevent ice condensation. The AARM was measured with AF demagnetizer/magnetizer LDA-3/AMU-1 and a JR-6 spinner magnetometer (AGICO Inc.) at the Geological Survey of Israel. Remanent magnetization was imparted in 12 pairs of antiparallel directions according to "A-mode" protocol with a DC field of 500 μT and AC field of 100 mT using the Rema6 software package. Magnetic fabric parameters were calculated according to Jelinek (1981) using the Anisoft 4.2 software package.

3.3. Magnetic Properties

To characterize the magnetic mineralogy of the rocks, a series of magnetic experiments were conducted on representative samples from each site. Alternating field demagnetization (AF) curves were measured in 10 to 20 mT steps from natural remanent magnetization up to 100 mT AC field. Isothermal remanent magnetization (IRM) curves were previously performed by Weinberger et al. (1997) for samples taken from the same sites as this study. After initial demagnetization in an AC field of 180 mT, the samples were subjected to stepwise remanence acquisition up to 900 mT and the magnetization was measured between each step. In addition, temperature-dependent susceptibility measurements (thermomagnetic curve) were measured with KLY-4S kappabridge and CS-3 furnace (AGICO Inc.) for temperature range between ~25 and 700 °C in an argon atmosphere.

4. Results

4.1. Magnetic Properties

The mean magnetic susceptibility (${k_m}^{RT}$) (Table 1 and Figure 4) at room temperature indicates that the studied intrasalt clastic beds have positive susceptibilities, between 5 and 250×10^{-6} SI with an average of $65 \pm 47 \times 10^{-6}$ SI.

The susceptibility increases significantly at low temperature (${k_m}^{LT}$), amplified by a factor of 3 to 3.9, excluding BC samples that are amplified by a factor of 2 to 3 (Table 1 and Figure 5). This amplification indicates a substantial contribution from paramagnetic minerals to the RT-AMS of the rocks (Issachar et al., 2018). The positive susceptibility values suggest that the contribution of diamagnetic minerals, such as quartz or calcite to the magnetic fabric is negligible. Therefore, ${k_m}^{LT}/{k_m}^{RT}$ ratios allow us to calculate the respective contribution of paramagnetic and ferromagnetic susceptibilities to the RT-AMS (for more information, see Issachar et al., 2016). The samples show dominancy of paramagnetic susceptibility (>70%) except for the BC samples, which display nearly equal contributions of paramagnetic and ferromagnetic susceptibilities (Figure 5b). For BD, samples diamagnetic contribution is not necessarily negligible, as ${k_m}^{RT}$ values are relatively low, thus the estimates presented in Figure 5b might be biased.

Remanence susceptibilities (k_R) show a linear correlation with room-temperature magnetic susceptibilities (${k_m}^{RT}$) (Figure 6). This indicates that the ferromagnetic minerals make an important contribution to the AMS of the studied rocks. Moreover, two distinct linear regression lines fit the samples. One regression line best fits the BD, BC, BN, and HS1 sites and displays a higher slope than the other, which best fits the HS2 and KA sites. This may indicate dissimilarity in magnetic mineralogy between these groups of rock samples.

The AF and IRM curves of the representative samples suggest three types of magnetic behavior: low coercivity minerals, probably carried by magnetite-titanomagnetite, which were fully demagnetized by AF treatment and fully saturated by IRM at ~200 mT (Figures 7a, 7b, and 8a); high-coercivity minerals, probably carried by hematite and/or goethite, which are not demagnetized by AF treatment and were not fully saturated by IRM at 900 mT (Figures 7c, 7d, and 8b); mixed-coercivity minerals, a combination of the

Table 1
RT-AMS, LT-AMS, and AARM Data

	RT-AMS						LT-AMS						AARM					
Site	N	k_m^{RT} (10^{-6} SI)	L	F	P	T	N	k_m^{LT} (10^{-6} SI)	L	F	P	T	N	k_R (10^{-6} SI)	L	F	P	T
BD	8	14.9 (1.4)	1.015 (0.005)	1.011 (0.005)	1.026 (0.005)	−0.16 (0.33)	5	49.0 (6.7)	1.018 (0.004)	1.004 (0.002)	1.022 (0.002)	−0.64 (0.24)	5	18.2 (2.0)	1.040 (0.009)	1.021 (0.006)	1.062 (0.009)	−0.29 (0.17)
BC	9	188.1 (36.3)	1.010 (0.004)	1.020 (0.010)	1.030 (0.012)	0.27 (0.26)	5	452.3 (88.2)	1.014 (0.005)	1.021 (0.010)	1.035 (0.013)	0.15 (0.29)	5	259.3 (74.3)	1.033 (0.009)	1.062 (0.025)	1.096 (0.021)	0.25 (0.28)
BN[a]	11	47.1 (2.1)	1.005 (0.002)	1.007 (0.003)	1.012 (0.002)	0.15 (0.37)	5	183.0 (3.1)	1.007 (0.002)	1.005 (0.001)	1.012 (0.003)	−0.19 (0.18)	5	60.8 (6.4)	1.027 (0.016)	1.034 (0.011)	1.061 (0.018)	0.17 (0.40)
HS1	11	85.5 (7.8)	1.005 (0.002)	1.009 (0.003)	1.014 (0.003)	0.28 (0.26)	5	307.9 (27.3)	1.009 (0.002)	1.012 (0.002)	1.021 (0.003)	0.12 (0.15)	5	108.2 (20.9)	1.029 (0.017)	1.048 (0.009)	1.079 (0.010)	0.28 (0.32)
HS2	14	49.4 (5.6)	1.002 (0.001)	1.003 (0.001)	1.004 (0.001)	0.19 (0.37)	5	164.8 (15.5)	1.002 (0.002)	1.003 (0.001)	1.005 (0.002)	0.23 (0.38)	5	20.0 (2.8)	1.023 (0.013)	1.016 (0.007)	1.039 (0.015)	−0.14 (0.43)
KA	8	112.1 (1.4)	1.001 (0.000)	1.008 (0.001)	1.010 (0.001)	0.70 (0.14)	5	346.3 (10.6)	1.004 (0.001)	1.018 (0.002)	1.022 (0.001)	0.65 (0.11)	5	39.1 (1.3)	1.018 (0.016)	1.050 (0.009)	1.069 (0.021)	0.56 (0.32)

Note. N = number of specimens; k_m = mean susceptibility; k_R = mean remanence susceptibility (in 10^{-6} SI units); L ($=k_1/k_2$) = magnetic lineation; F ($=k_2/k_3$) = magnetic foliation (e.g., Tarling & Hrouda, 1993); P = degree of anisotropy; T = shape ellipsoid. Standard deviations (sigma) are in parentheses.
[a]Samples from Unit 1 only.

aforementioned behaviors, in which the rocks are partially demagnetized by AF treatment and have not been completely saturated by IRM at 900 mT (Figures 7e, 7f, and 8c).

The thermomagnetic curve of a representative sample from site HS1 indicates a monotonic decrease at heating, although a notable drop occurs at 500 °C and a cooling curve indicates reversibility up to that point (Figure 9a). This may indicate the presence of titanomagnetite minerals. The thermomagnetic curve of a representative sample from site HS2 indicates a gentle decrease at heating up to ~500 °C, increase up to 565 °C, and a drop up to 600 °C, and cooling curve indicates reversibility up to 580 °C (Figure 9b). These may be related to the presence of magnetite minerals. The thermomagnetic curve of a representative sample from site BC shows a monotonic decrease at heating up to 530 °C, a major drop between 530 and 580 °C on heating and reversibility in cooling up to 580 °C, indicating substantial presence of magnetite and titanomagnetite grains (Figure 9c).

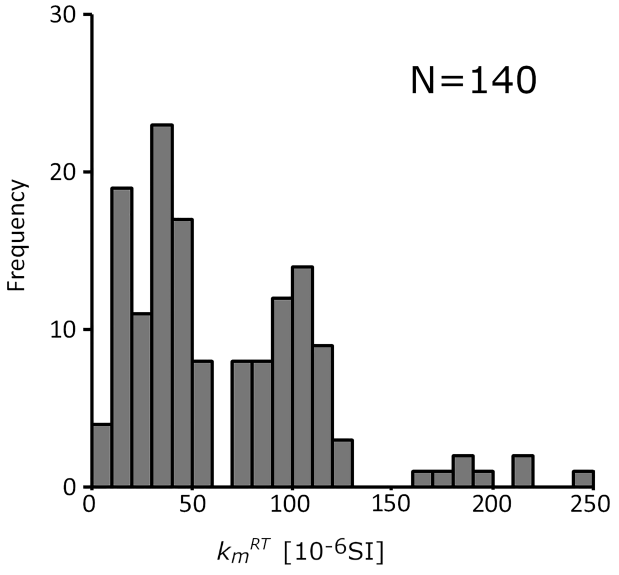

Figure 4. Frequencies of mean susceptibilities (k_m^{RT}) of 140 studied samples.

4.2. Magnetic Fabrics

The *T*-*P* diagrams (shape versus degree of anisotropy) of samples that were measured for both RT-AMS, LT-AMS, and AARM are presented in Figure 10. The RT-AMS and LT-AMS plots are quite similar and characterized by low P values (1.016 ± 0.009, see Table 2) and varied T values, between oblate ($T = 1$) to neutral ($T = 0$) shapes, where LT-AMS fabrics commonly has slightly lower T values. The AARM parameters are characterized by P values between 1.03 and 1.15 and T values between oblate ($T = 1$) and prolate ($T = -1$) (Figure 10c, Table 1).

The principal susceptibility axes of RT-AMS, LT-AMS, and AARM fabrics are presented in Figure 11 and Table 2. The magnetic fabrics of sites BD, BC, and BN of the Bnot Lot shale member are characterized by clusters of three susceptibility axes (triaxial fabrics), although AARM of BD and BN sites show less-clustered axes. The magnetic fabrics show a strong relation to bedding as $\boldsymbol{K_3}$ (or $\boldsymbol{K_{R3}}$) axes are normal to bedding plane at each site, and $\boldsymbol{K_1}$ (or $\boldsymbol{K_{R1}}$) are typically oriented subparallel to the strike of beds.

The magnetic fabrics of site HS1 are triaxial and $\boldsymbol{K_3}$ axes are normal to bedding plane. The RT-AMS, LT-AMS and AARM fabrics at this site indicate similar orientations, although $\boldsymbol{K_{R1}}$ and $\boldsymbol{K_{R2}}$ axes of the AARM fabric are switched relative to the RT-AMS and LT-AMS fabrics. The $\boldsymbol{K_1}$ axes of

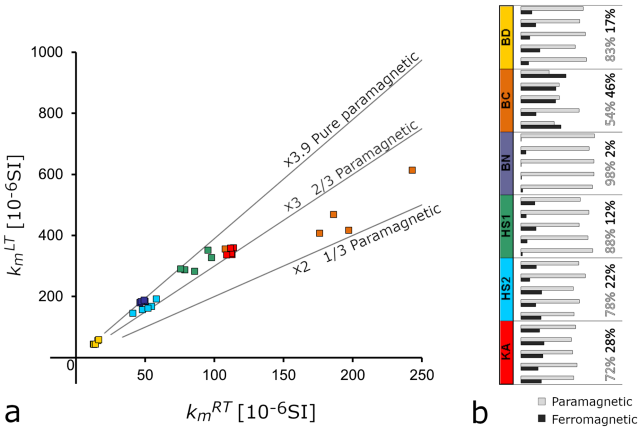

Figure 5. (a) Low-temperature mean susceptibility (k_m^{LT}) versus room-temperature mean susceptibility (k_m^{RT}) of the intrasalt beds. The gray lines represent theoretical relations of paramagnetic and ferromagnetic minerals in the sample, assuming no contribution from diamagnetic minerals (see Cifelli et al., 2005). (b) Calculated paramagnetic and ferromagnetic contributions to k_m^{RT}.

RT-AMS and LT-AMS fabrics are oriented parallel to the bedding strike in a NNW direction with very shallow (<5°) inclinations. Conversely, the magnetic fabrics of site HS2 show quite scattered axes. The RT-AMS indicates that mean $\boldsymbol{K_3}$ axes are oriented normal to bedding, and the mean $\boldsymbol{K_1}$ axes is scattered along the WNW-ESE direction.

The magnetic fabrics of site KA are triaxial and show no obvious relations to bedding. RT-AMS, LT-AMS, and AARM fabrics show quite similar orientations, but $\boldsymbol{K_2}$ ($\boldsymbol{K_{R2}}$) and $\boldsymbol{K_3}$ ($\boldsymbol{K_{R3}}$) axes of the AARM fabric are switched relative to the RT-AMS and LT-AMS fabrics.

The RT-AMS results of the different rock units at site BN are shown in Figure 12. The susceptibility values vary between 12.7 and 111.9×10^{-6} SI, testifying to the difference in mineral composition between the units. The T values show oblate ($T = 1$) to neutral ($T = 0$) shapes and $P < 1.03$. The principal AMS axes of the different units show similar orientations as $\boldsymbol{K_3}$ axes are normal to bedding and $\boldsymbol{K_1}$ and $\boldsymbol{K_2}$ axes are within the bedding plane. Although Units 5 and 6 show quite scattered orientations, the lithology and composition generally have little effect on AMS, which is controlled by structure and deformation. We regard Unit 1 as a representative magnetic fabric for the BN site (Table 1).

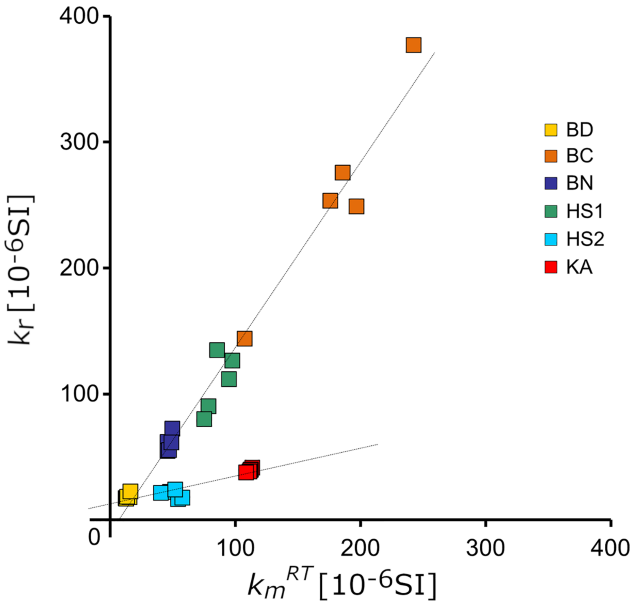

Figure 6. Remanence susceptibility (k_R) versus room-temperature mean susceptibility (k_m^{RT}) of the intrasalt beds.

5. Discussion

5.1. Characteristics of the Magnetic Fabrics

In this study, we analyzed the magnetic fabrics of 140 samples collected from six sites within intrasalt beds (mainly clastic rocks) along the exposed Sedom salt wall. Our analysis shows that both paramagnetic and ferromagnetic minerals contribute to the magnetic fabrics, yet the paramagnetic contribution to the RT-AMS is commonly much higher than that of the ferromagnetic minerals (Figure 5b). Notably, LT-AMS fabrics are generally similar to the RT-AMS fabrics but display a slightly stronger anisotropy and more clustered susceptibility axes (Figures 10 and 11). The dominancy of the paramagnetic contribution to the AMS of sedimentary rocks is reported in previous studies in general (e.g., Parés, 2015, and references therein) and in studies of intrasalt beds in particular (Santolaria et al., 2015; Soto et al., 2014). The paramagnetic minerals in the clastic units of the Sedom Formation are mostly clays of the illite and kaolinite groups (Zak, 1967 p. 35). Hence, it is likely that the RT-AMS and LT-AMS reflect the preferred orientation of phyllosilicates, which is

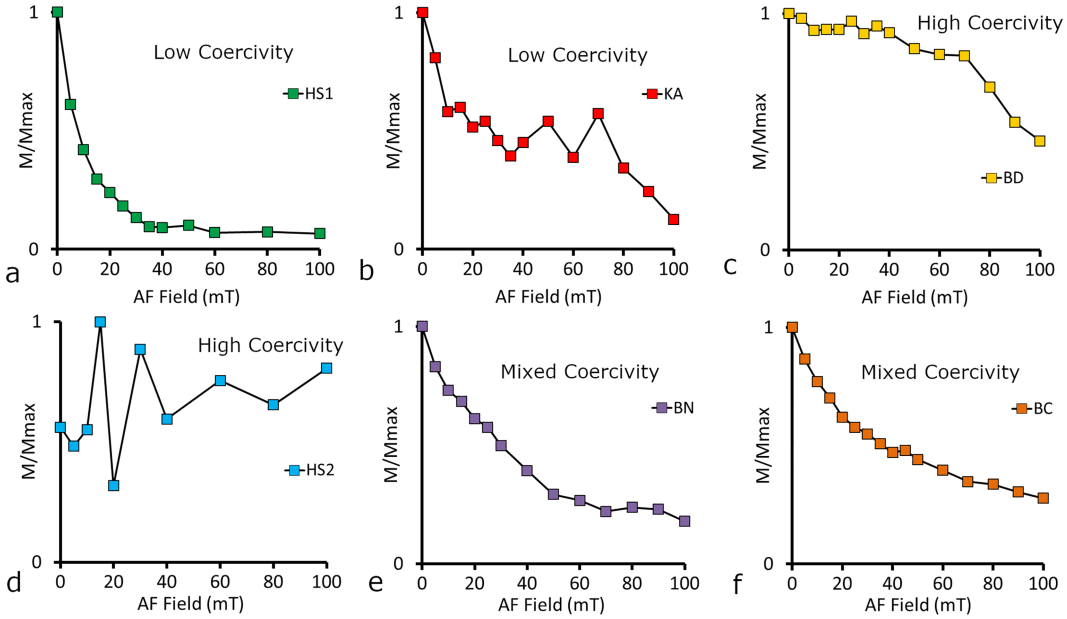

Figure 7. Alternating field (AF) demagnetization curves of selected samples.

acquired by accommodation of grain slippage and rotation, and intragranular kinking and deformation bends of the clay minerals (Borradaile & Tarling, 1981; Milliken & Reed, 2010; Oertel, 1983; Parés et al., 1999; Parés & van der Pluijm, 2002a; van der Pluijm & Kaars-Sijpesteijn, 1984). This is with agreement with previous studies that have shown that magnetic fabrics mimic the preferred orientation of phyllosilicates (Borradaile & Werner, 1994; Chadima et al., 2004; Hrouda et al., 1997; Parés & van der Pluijm, 2002b). Samples of BC site display nearly equal contributions of paramagnetic and ferromagnetic susceptibilities to the RT-AMS (Figure 5). Moreover, the RT-AMS, LT-AMS, and AARM fabrics are similar (Figure 11), indicating that the ferromagnetic and paramagnetic minerals acquired similar magnetic fabrics under deformation conditions.

The magnetic fabrics of sites BD, BC, BN, HS1, and HS2 show common triaxial characteristics with clusters of $\boldsymbol{K_3}$ axes normal to the bedding planes and clusters of $\boldsymbol{K_1}$ and $\boldsymbol{K_2}$ axes within these planes. In light of models describing progressive evolution of magnetic fabrics in sedimentary rocks (e.g., Parés et al., 1999; (e.g., Parés et al., 1999; Aubourg et al., 2004), the magnetic fabrics of the intrasalt beds show imprint of tectonic deformation (i.e., shortening) in addition to the initial deposition fabric. According to these models, clusters of $\boldsymbol{K_3}$ axes are formed normal to bedding early in the consolidation and lithification stages by face-to-face alignment of phyllosilicates (Bennett et al., 1981). In the early stages of tectonic deformation, clusters of $\boldsymbol{K_1}$ and $\boldsymbol{K_2}$ axes are formed within the bedding plane. The $\boldsymbol{K_1}$ axes are oriented along the intersection of bedding and the tectonic flattening planes and therefore define the trend of tectonic extension within the plane of bedding (see Parés, 2015, for review). The magnetic fabrics of site KA are exceptional as they do not show an affinity to bedding. This could be attributed to a tectonic fabric that completely obliterated the initial deposition fabric (Parés et al., 1999) or to an inverse fabric that evolves as a result of specific mineralogy

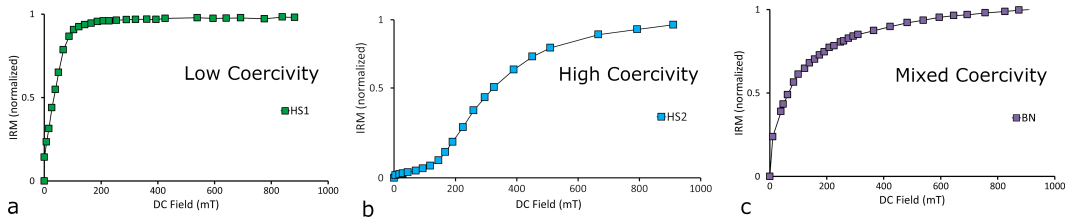

Figure 8. Isothermal remanent magnetization (IRM) curves of selected samples.

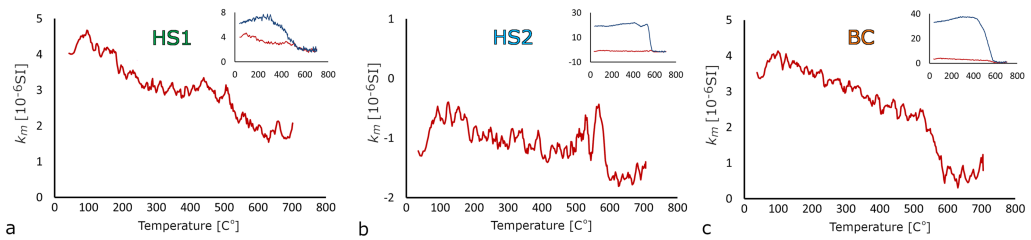

Figure 9. Temperature-dependent susceptibility measurements (thermomagnetic curves) of selected samples showing heating (red) and cooling (blue) runs. The red curves in the large and small figures are the same.

(Rochette, 1988). In the case of inverse fabrics we would expect $\boldsymbol{K_1}$ axes to align perpendicular to bedding and $\boldsymbol{K_2}$, $\boldsymbol{K_3}$ axes to lie within the plane of bedding. Because the AMS axes are oriented differently, we prefer the tectonic model over that of the inverse fabric. Nevertheless, the lack of additional sampling sites from the southern parts of the salt wall hampers a clear resolution of the origin of the KA fabric.

5.2. Relationships of Magnetic Fabrics to Structural Elements of the Sedom Salt Wall

In order to correlate the magnetic fabrics with salt flow processes, we need to determine the timing of magnetic fabric acquisition relative to salt wall emplacement stages. We also need to appreciate the kinematics and mechanical significance of magnetic fabrics by considering these results in the context of structural features within the Sedom salt wall.

5.2.1. Magnetic Fabrics and the Bnot Lot Recumbent Fold

The Bnot Lot shales are folded into a major recumbent fold, the Bnot Lot fold, in the northeastern flank of the Sedom salt wall. Alsop et al. (2015) calculate from measurements of bedding around the Bnot Lot fold that the hinge plunges gently toward the NW (15°/315°). They suggest that the Bnot Lot fold must have been formed by processes operating within the salt wall itself, as no regional compression has operated in the Dead Sea Basin since deposition of the Sedom Formation. On the contrary, the Sedom salt wall is located along a releasing bend of the DSF (Smit et al., 2008), and the region has been subjected to E-W extension during the growth of the Sedom salt wall since the Pliocene (Garfunkel, 1981; Sagy et al., 2003). Several observations led Alsop et al. (2015) to suggest that the Bnot Lot fold was generated by flow of extruded salt, which moved gravitationally downslope over the Bnot Lot shales. These observations include the parallelism of the fold hinge and the strike of the paleoslope, and preservation of caprock directly above the Bnot Lot shales, indicating that soluble salt must have originally been positioned above the shales. In addition, the thickness of the Bnot Lot shales is constant around the fold, the overturned upper limb is thrust and placed directly on overburden units, and NE verging folding and thrusting has been superimposed on all units along the northeastern flank of the salt wall. Alsop et al. (2015) suggest that the fold can be described mechanically by a "rolling hinge" model (e.g., Graham et al., 2012), in which the rocks of the overturned upper limb had passed and folded around the hinge zone, before flowing down the paleoslope toward the NE. In this model, rocks forming the steep lower limb never reached the hinge zone and therefore should not be influenced by it.

Sites BD and BC are within the overturned upper limb of the Bnot Lot fold, whereas sites BN, HS1, and HS2 are within the steep lower limb. Notably, the in situ magnetic fabrics indicate that the mean $\boldsymbol{K_1}$ axes of sites

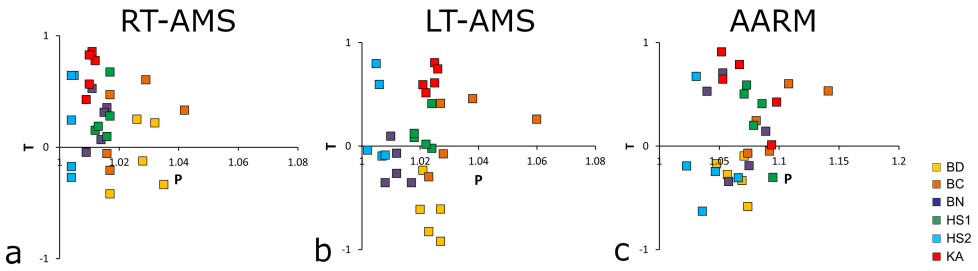

Figure 10. *T-P* diagrams for RT-AMS, LT-AMS, and AARM fabrics. Sampling sites are indicated by different colors.

Table 2
Mean Tensors Principal Orientations (in Dip/Dip Direction Format) and Their 95% Bootstrap Confidence Cones (Maximum/Minimum) of RT-AMS, LT-AMS, and AARM

	RT-AMS			LT-AMS			AARM		
	Principal axes - trend/plunge (95% Conf. angles - max/min)			Principal axes - trend/plunge (95% Conf. angles - max/min)			Principal axes - trend/plunge (95% Conf. angles - max/min)		
Site	K_1	K_2	K_3	K_1	K_2	K_3	K_{R1}	K_{R2}	K_{R3}
BD	01/311 (10/5)	11/221 (10/8)	79/042 (9/7)	08/308 (11/3)	08/216 (19/10)	72/063 (19/3)	11/262 (24/11)	05/171 (34/17)	77/058 (31/13)
BC	17/311 (9/6)	12/317 (8/4)	69/092 (7/4)	19/307 (5/3)	11/213 (6/1)	68/093 (5/2)	03/319 (8/4)	20/228 (9/3)	70/058 (9/7)
BN[a]	24/323 (14/5)	51/087 (14/9)	28/219 (9/5)	28/322 (5/4)	50/092 (10/5)	25/216 (11/4)	09/317 (16/2)	59/063 (18/13)	30/222 (16/6)
HS1	02/339 (9/4)	53/247 (9/6)	37/071 (6/5)	01/334 (6/2)	46/243 (7/5)	44/066 (7/4)	59/245 (12/2)	02/152 (11/2)	35/060 (8/2)
HS2	22/273 (52/8)	63/127 (53/22)	13/009 (25/9)	41/184 (22/3)	27/301 (25/21)	37/053 (25/5)	34/084 (25/16)	28/331 (76/16)	42/210 (76/19)
KA	55/045 (11/2)	13/296 (11/2)	32/198 (3/1)	38/080 (9/2)	38/313 (9/3)	30/196 (4/1)	53/014 (29/2)	35/211 (29/2)	08/115 (8/2)

[a]Samples from Unit 1.

BD, BC, and BN are parallel to the direction of the Bnot Lot fold hinge (Figure 13a). In order to shed more light on the geometrical relations between the magnetic fabrics and the salt wall we restored the tilted beds and their associated AMS axes back to horizontal in two different ways: (1) Restoration relative to the bedding strike, that is, all the data were rotated to a paleohorizontal surface (rotations performed counterclockwise along strike when looking toward the NW) (Figure 13b). Such rotation leads to clustering of AMS axes, excluding site BC. (2) Restoration relative to the Bnot Lot fold to a horizontal surface (achieved first by rotation around the fold hinge (15°/315°), depending on the limb dip, and then counterclockwise rotation of 15° around a horizontal axis (00°/225°)). This leads to clustering of AMS axes, excluding site HS1 (Figure 13c). The best clustering of AMS axes is obtained by a restoration of sites BD and BC (from the overturned upper limb) relative to the fold hinge and sites BN, HS1, and HS2 (from the steep lower limb) around bedding strike (Figure 13d). Using both techniques, the mean $\boldsymbol{K_3}$ axes show vertical clustering normal to the horizontal bedding.

The tectonic fabrics of sites from the steep lower limb are better grouped after restoration around bedding strike rather than restoration relative to the Bnot Lot fold hinge (BN, HS1, and HS2 in Figure 12b). This suggests that the tectonic fabrics were developed prior to the Bnot Lot folding and at a similar bedding position. On the other hand, the tectonic fabrics from the overturned upper limb are better grouped after restoration around the fold hinge (BD and BC in Figure 13c), suggesting that these sites participated in the Bnot Lot folding. Moreover, they are restored to a similar orientation as the sites of the steep lower limb. This implies that the magnetic fabrics of the overturned upper limb were also initially developed at similar bedding orientations to those of the steep lower limb and, thus, prior to the Bnot Lot folding. Subsequently, the rocks of the overturned upper limb have passed around the "rolling hinge" and were further deformed with magnetic fabrics characterized by (1) parallelism of the in situ $\boldsymbol{K_1}$ axes to the fold hinge and $\boldsymbol{K_2}$ axes to the NE verging folding and thrusting (see BD and BC sites at Figure 11) and (2) higher degree of anisotropy in comparison with samples from the lower limb (P values are 1.028 and 1.010, respectively, BD and BC sites at Figure 10a and Table 1).

We note that the direction and amount of rotation is highly reliant on the identification at each site of the correct "way up" of the section (i.e., top versus bottom of the section). In sites were the section is overturned, the rotations were performed around the obtuse (>90°) angle to restore it back to horizontal. In addition, we note that the restorations performed above follow practices that are commonly used in paleomagnetic studies, in which the magnetic vectors serve as passive markers during rotations (e.g., Weinberger et al., 1995). However, the AMS axes in this case cannot be considered as "passive markers" as their alignments and clustering have varied inelastically during deformation within the rock mass. Nevertheless, these nonphysical restorations seem to shed light on the geometrical relations between the magnetic fabrics and the structure.

5.2.2. Magnetic Fabrics and Paleomagnetic Vectors

Weinberger et al. (1997) measured the paleomagnetic data of clastic rocks within the Sedom salt wall and demonstrated that two magnetic remanence components may be distinguished in these rocks. A high-coercivity component, which was acquired prior to tilting of the beds by detrital remanent magnetism

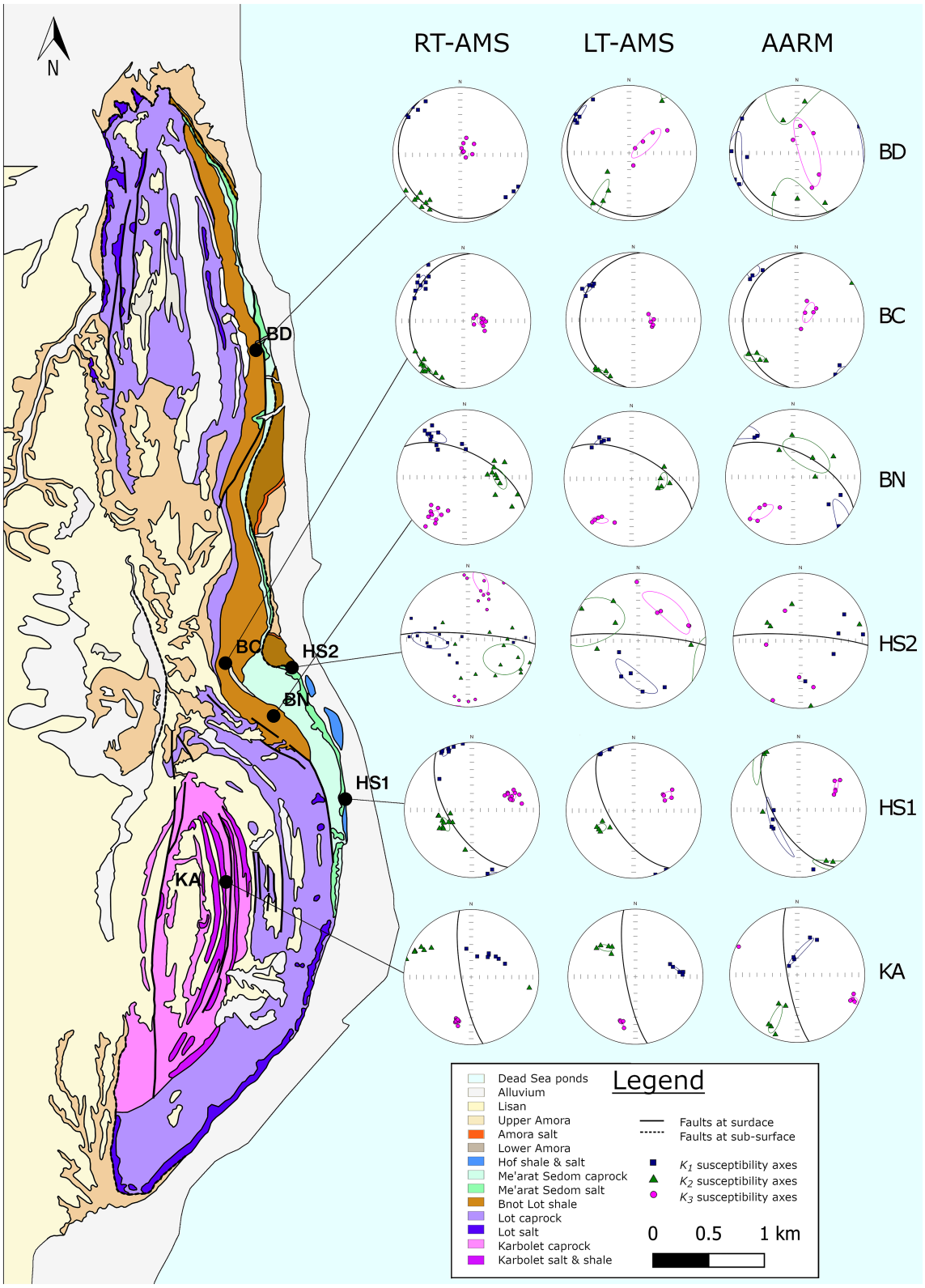

Figure 11. Geologic map of the Sedom salt wall (Agnon et al., 2006) and sampling sites for magnetic fabrics (AMS, LT-AMS, and AARM), which are lower hemisphere, equal-area projections of susceptibility principal axes, and their 95% confidence ellipses. Black great circles correspond to bedding planes.

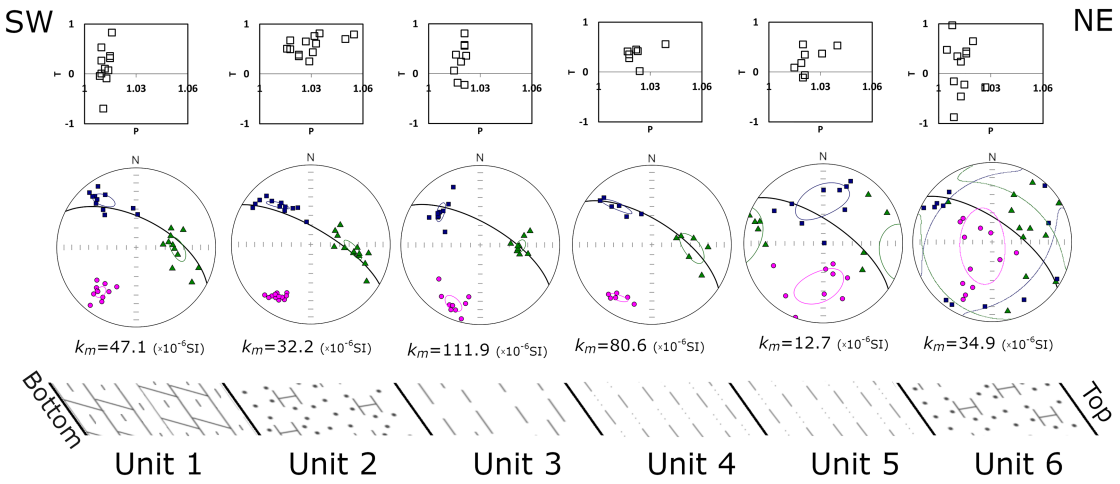

Figure 12. RT-AMS fabrics for different rock types at site BN. (top) *T-P* diagrams. (middle) Lower hemisphere, equal-area projection of AMS principal axes, and their 95% confidence ellipses. Black great circles correspond to bedding planes (68°/035°). (bottom) Schematic cross section (not to scale) showing general bedding orientation and rock units. The rock types are listed in section 3.1.

acquisition, and a low-coercivity component, which is secondary and was acquired after tilting of the beds by chemical remanent magnetism acquisition. The low-coercivity component is carried by an authigenetic magnetite that was probably formed after the piercing diapir reached the water table or even later when it had been exposed to atmospheric conditions. In the current study, the AARM data mostly reflects the magnetic fabric of low-coercivity minerals, as the high-coercivity minerals are not fully demagnetized by an applied field of 100 mT (see section 3.2). The AARM fabrics comprise clusters of $\boldsymbol{K_3}$ axes that are normal to bedding, and in general, their principal directions are coaxial with the AMS fabrics. This suggests that the newly formed low-coercivity Fe minerals mimic the magnetic fabric of the high-coercivity Fe minerals that were tectonically acquired prior to the chemical remanent magnetism acquisition. Ebert et al. (2018) showed by high-resolution electron probe microanalysis and magnetic force microscopy techniques that magnetic grains, which formed by mineral alteration after sedimentation, mimic the shape and geometry of the initial Fe-Ti grains. They show that iron sulfides, which altered titanomagnetite grains, preserve the shape of the initial Fe-Ti grains, but acquire a secondary magnetization. Accordingly, the current AARM results may demonstrate how the newly formed low-coercivity minerals preserve and reflect the magnetic fabrics, even though they were acquired later as a secondary phase.

5.2.3. Magnetic Fabrics and Salt Wall Structure

The orientation of the magnetic fabrics in the salt wall cannot be the result of the Dead Sea stress field in this area (~NNW-SSE maximum horizontal shortening, see Eyal & Reches, 1983), which is in contrast to magnetic fabrics within sedimentary rocks from adjacent areas along the DSF (Issachar et al., 2019). Rather, we interpret the magnetic fabrics to reflect inelastic deformation within the intrasalt beds that developed during salt wall emplacement.

A very prominent feature of the magnetic fabrics is the orientations of $\boldsymbol{K_1}$ axes along the bedding strike (Figure 11). The steep inclinations and the overturned strata of the beds in the exposed salt wall indicate they underwent substantial tilting of 70° to 200°. The parallelism of $\boldsymbol{K_1}$ axes and bedding strike suggests that the beds underwent folding about bedding strike, and by that clusters of $\boldsymbol{K_1}$ axes were consequently formed. Clustering of $\boldsymbol{K_1}$ axes along the bedding strike during folding are commonly observed during inelastic deformation of soft sediment mass transport deposits (Levi et al., 2018; Weinberger et al., 2017).

Note, that in sites BC, BN and HS2, which are in the "pinched" central area and close to the hinge zone of the Bnot Lot fold, clusters of $\boldsymbol{K_1}$ axes are characterized by shallow inclinations (~30°). This can be explained by a local noncylindrical folding effect, in which bedding strike and the hinge line are not parallel to one another close to the hinge zone. In that manner, $\boldsymbol{K_1}$ axes at these sites migrated toward the intersection of bedding and the tectonic flattening plane (i.e., fold axial plane). Noncylindrical folding culminating in highly curvilinear sheath folds is commonly recorded by marker beds across a range of scales within salt (e.g., Alsop et al., 2007).

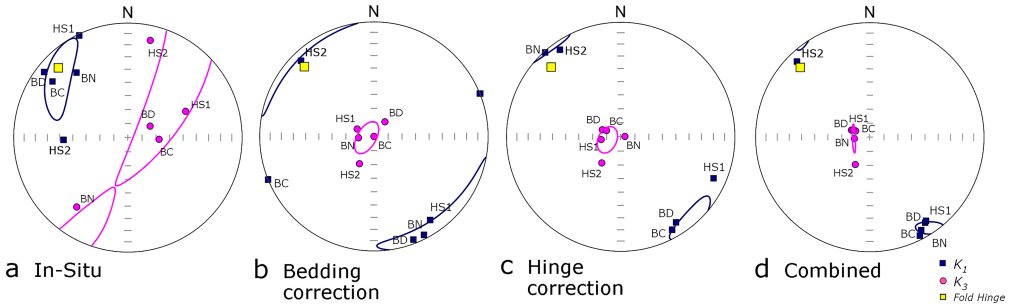

Figure 13. Lower hemisphere, equal-area projection of mean AMS principal axes in sites BD, BC, BN, HS1, and HS2, and their 95% confidence ellipses. Yellow square indicates the trend of Bnot Lot fold hinge (15°/315°) (Alsop et al., 2015). (a) In situ magnetic fabrics. (b) AMS axes rotated around the bedding strikes. (c) AMS axes restored relative to the Bnot Lot fold, first by rotation around the fold hinge (15°/315°) and then around horizontal axis (00°/225°). (d) AMS axes of sites BN, BC, and BD restored relative to the Bnot Lot fold and of sites HS1 and HS2 rotated around the bedding strike.

5.2.4. Timing of Magnetic Fabric Acquisition

Based on the relationships between the magnetic fabrics and structural features within the Sedom salt wall, described in sections 5.21–5.2.3, several constraints can be imposed regarding the timing of magnetic fabric acquisition relative to various "milestones" of Sedom salt wall emplacement:

1. The alignment of $\boldsymbol{K_3}$ axes normal to bedding most likely preserves the depositional imprint that was acquired during the early stages of intrasalt bed diagenesis.
2. The triaxial fabrics indicate that tectonic fabrics were acquired after deposition and during deformation of the intrasalt beds.
3. The orientation of $\boldsymbol{K_1}$ axes along bedding strike suggests that the magnetic fabrics were acquired by folding of the intrasalt beds from horizontal to their present steeply dipping or overturned attitudes during salt tectonic processes.
4. The clustering of the restored AMS axes suggests that the magnetic fabrics were acquired before the formation of the Bnot Lot recumbent fold (Figure 13).
5. The parallelism of the $\boldsymbol{K_1}$ axes to the trend of the Bnot Lot fold hinge, the parallelism of the in situ $\boldsymbol{K_2}$ axes to NE verging folds and thrusts, and the slightly higher degree of anisotropy in sites from the overturned upper limb of the Bnot Lot fold (in comparison with the lower steep limb) suggest that the magnetic fabrics were further deformed during this later folding.

5.3. Kinematic and Mechanical Implications of the Magnetic Fabrics

Studies show that phyllosilicates more easily form tectonic magnetic fabrics under some overburden (i.e., lithostatic pressure) and increased pore fluid pressure, as the rocks are weakened and micro-deformation mechanisms operate more efficiently (Maltman & Bolton, 2003; Parés, 2015). Such conditions might prevail during the emplacement of the Sedom salt wall as inferred from subsurface data. The seismic section that crosses the center of the exposed Sedom ridge shows that the geometry of the salt wall varies with depth. It is narrow (<1 km) at a depth of ~3- to 2-s TWT, where a necked region is observed against the subsurface normal Sedom Fault (Figure 1b). The salt wall is much wider (>2 km) between 2- and 0.5-s TWT, and about 2 km wide close to the surface (e.g., Al-Zoubi & ten Brink, 2001; Gardosh et al., 1997; Larsen et al., 2002) (Figure 1b). While the necked region is viewed in 2-D in the seismic section, in 3-D view based on the top salt map of Al-Zoubi and ten Brink (2001), it may be visualized as a long and narrow region that parallels the trend of the Sedom Fault in the subsurface (Larsen et al., 2002). The trend of this fault varies but follows a NNW trend underneath the northern part of the mountain. The rocks in a necked region experience high stress (e.g., Davison et al., 1996), which could be accompanied by increased fluid pressure and thus conditions preferable for mineral alignment and tectonic magnetic fabric acquisition in the intrasalt beds. Although the orientation of beds cannot be seismically imaged within the salt mass, it is likely that the intrasalt beds gradually change their orientation from subhorizontal to subvertical in the necked region. Consequently, the intrasalt beds are subjected to normal flattening and to along-strike extension, parallel to the fold axis (Fossen, 2016). In this region, tectonic magnetic fabrics could be acquired with $\boldsymbol{K_1}$ axes along the trend of

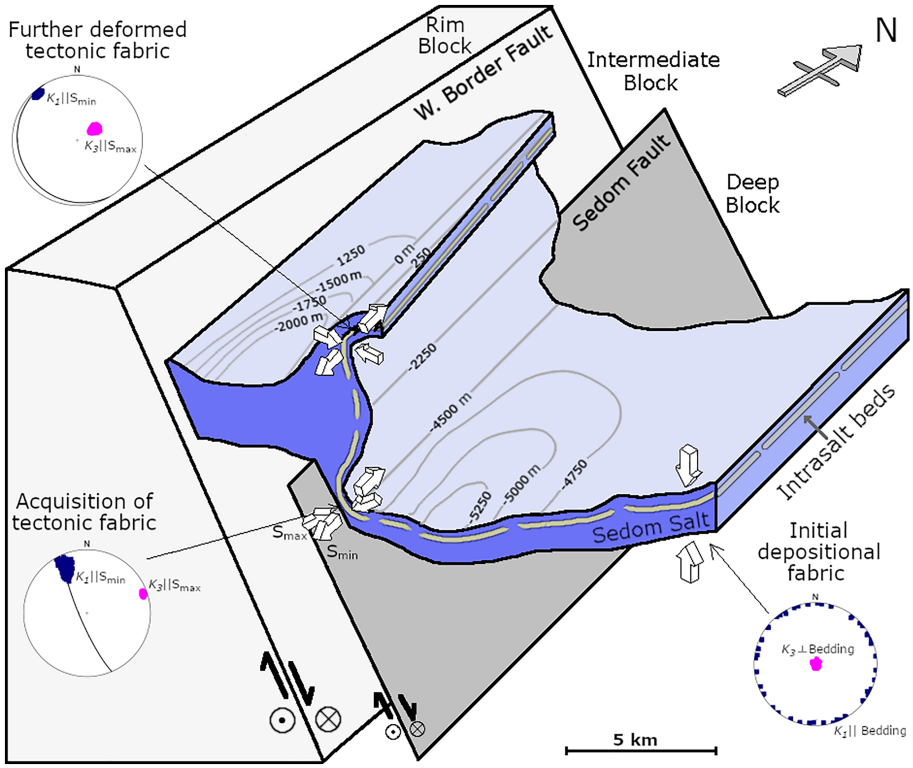

Figure 14. Scaled 3-D model of the Sedom salt wall showing three regions of magnetic fabric acquisition. In this image overburden layers are not shown. Arrows indicate the maximum extension (S_{max}) direction, parallel to $\boldsymbol{K_3}$ axes and minimum shortening (S_{min}) direction, parallel to $\boldsymbol{K_1}$ axes. Contours mark the depth to top Sedom Formation (modified from Al-Zoubi & ten Brink, 2001), which refers to datum −400 msl. The intrasalt beds form a stinger of large boudins (schematically) in the subsurface.

the neck, which mimics the trend of the Sedom Fault, and results in $\boldsymbol{K_1}$ axes parallel to the strike of the Sedom Fault and $\boldsymbol{K_3}$ axes normal to bedding and to the fault plane (Figure 14).

The Sedom salt wall is considered to have undergone stages of both passive and active diapirism (Alsop et al., 2016). However, it is likely that reactive diapirism developed at its initial stage in association with the fault system of the Dead Sea Basin. We suggest that the tectonic magnetic fabrics of the intrasalt beds were acquired at depth during prolonged passive diapirism and salt wall growth, in association with folding along the necked region in the subsurface. During the later active stages, the intrasalt beds were brought to the surface within the flowing salt mass from a burial depth of at least a few hundred meters. During this stage the magnetic fabrics of the intrasalt beds have not recorded the vertical flow of the surrounding salt mass and intrasalt beds may be considered as "rafts" transported by the surrounding flowing salt mass. We emphasize that the fabrics have not been obliterated by this active stage, as suggested by clustering of $\boldsymbol{K_3}$ axes normal to bedding. During salt extrusion, the intrasalt beds experienced further major folding and growth of the Bnot Lot recumbent fold. The fold formed below a surficial salt glacier that flowed toward the basin depocenter (Alsop et al., 2015), NE of the Sedom salt wall (Larsen et al., 2002). The trend of the Bnot Lot fold thus resembles the trend of the subsurface fold at the necked region. The intrasalt beds that participated in this folding were therefore further deformed (Figure 14; section 5.3).

5.4. Role of Intrasalt Beds as a Deformation Marker

The ~200-m-thick Bnot Lot shale member was deposited in the upper section of the Sedom Formation and forms intrasalt beds between the Lot and Me'arat Sedom salt members (Zak, 1967). The shale units can therefore be regarded as being thick and relatively competent intrasalt beds within a weak salt mass. Studies have shown that the deformation of intrasalt beds depends on their thickness. Thin centimeter-scale intrasalt beds tend to reflect complex flow patterns of the host rock salt (Burliga, 2014, 2018; Sans et al., 1996), whereas thick intrasalt beds, of meters to hundred-meter scale, form independent mechanical units

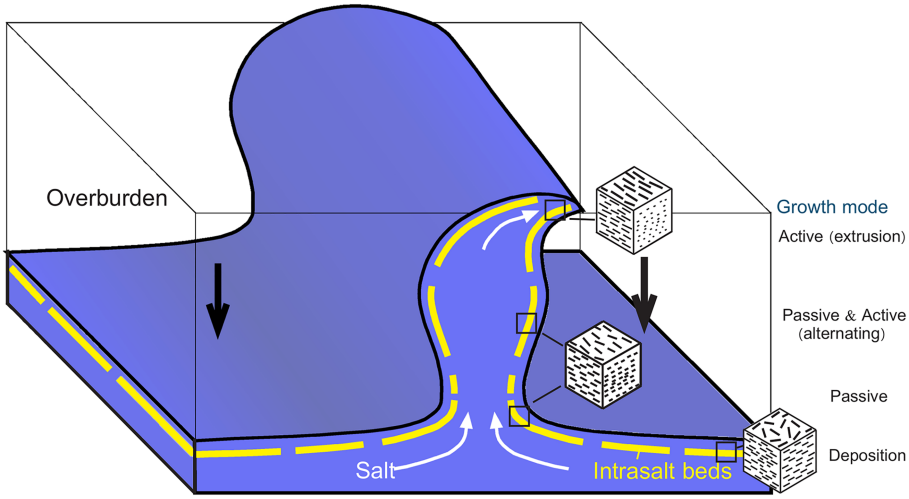

Figure 15. Conceptual model for the internal deformation of thick intrasalt beds (yellow) during salt wall growth. The cubes illustrate the rock texture by means of mineral alignment. The internal deformation is initially developed during passive diapirism at the base of the salt wall as the beds fold in a necked region. The internal deformation is generally oblivious to the upward vertical rise of the beds. During salt extrusion, the internal deformation may increase by folding at the surface.

as imaged on high-resolution seismic (Jackson et al., 2014; Rowan et al., 2019; Van Gent et al., 2011). Observations (e.g., Borchert & Muir, 1964; Jackson et al., 2014; Li et al., 2012; Strozyk et al., 2012), supported by numerical models (e.g., Koyi, 2001; Rowan et al., 2019) show that thick intrasalt beds typically boudinage and/or fold during passive diapiric processes. Li (2016) shows that for shallow intrasalt beds positioned close to the top of sections, the first breaks and separation of boudins occur soon after the start of the downbuilding process. The shale units exposed along the Sedom wall are therefore not necessarily continuous in the subsurface but part of a large-scale (>1 km) stringer of boudins (Figure 14). Moreover, the Bnot Lot shale member is also not continuous when traced to the south along the exposed ridge (Figure 1c).

Previous studies show that thin (centimeter scale) intrasalt beds within the Sedom Formation reflect vertical extension, which is directly related to vertical flow of the encasing salt (Alsop et al., 2015; Zak & Freund, 1980). In this study, we show that the internal deformation of the thick intrasalt beds is related to major folding events that occurred during the early stages of salt tectonic processes and have not been overprinted by later extensive vertical flow of the surrounding salt. Hence, the present study highlights the difference in the style of deformation between thick and thin intrasalt beds.

In summary, we suggest a general model for the development of internal deformation within thick intrasalt beds during salt tectonic processes (Figure 15). During the initial stages of salt flow, the thick intrasalt beds may boudinage without significant accumulation of internal deformation. Internal deformation is initially developed within these beds during early stages of passive and/or reactive diapirism, as the beds are tilted and folded from their original horizontal attitude to a subvertical position. In the case of elongated structures such as salt walls, an extension is developed parallel to the trend of the fold axis. During active diapirism and upward salt flow, the "rafts" (i.e., large-scale boudins) of the intrasalt beds are uplifted and carried with the encasing salt; however, negligible internal deformation is being developed. During salt extrusion, further internal deformation may be accumulated by near-surface folding as a result of gravity-driven salt flow. The flow is toward the depocenter from which salt withdraw into the salt wall, and, consequently, the trend of the surficial fold resembles and mirrors that of the subsurface fold (Figure 15).

6. Conclusions

We studied thick (~200 m) intrasalt beds within a rock salt mass in order to elucidate the role played by these beds during passive and active diapirism. We investigated the deformation of these beds by measuring the magnetic fabrics of samples from six sites along the Sedom salt wall. The main conclusions of the study are as follows:

- The magnetic fabrics reflect phyllosilicate preferred orientation and characterized by triaxial fabrics with mean susceptibility values of $k_m = 65 \pm 47 \times 10^{-6}$ SI, oblate to neutral shape of anisotropy ($0 < T < 1$) and low degree of anisotropy ($P = 1.016 \pm 0.009$).
- The orientations of the principal susceptibilities and the anisotropy parameters are controlled by structure and deformation rather than lithology (e.g., siltstones, evaporates, and clay), and thus, the magnetic fabrics could be used as kinematic markers.
- The magnetic fabrics shows tectonic imprints (clusters of $\boldsymbol{K_1}$ and $\boldsymbol{K_2}$ axes) in addition to the initial deposition fabrics (clusters of bedding-normal $\boldsymbol{K_3}$ and girdle of $\boldsymbol{K_1}$ and $\boldsymbol{K_2}$ axes). The $\boldsymbol{K_1}$ axes were reoriented parallel to the trend of tectonic extension within bedding planes, as the beds underwent folding about the bedding strike.
- We suggest that the tectonic fabrics were initially acquired at the necked region in association with the subsurface Sedom Fault at the base of the salt wall. These developed during passive diapirism, which was associated with folding of the beds from the horizontal to the vertical. Later, active diapirism brought the intrasalt beds to the surface but has not obliterated the magnetic fabrics acquired earlier in the passive stage.
- During salt extrusion, the rocks of the overturned upper limb of a large-scale recumbent fold (the Bnot Lot fold) were further deformed near the surface by gravity-driven folding at the base of a salt glacier.
- The internal deformation of thick intrasalt beds is related to major folding during salt wall growth. The thick intrasalt beds are mechanically distinct from the flowing salt and preserve information on salt tectonic processes operating at depth.

Acknowledgments
This study was supported by grants from the Israel Science Foundation (ISF Grant 868/17) and the Israeli Government (under the Geological Survey of Israel, Dead Sea, project 40706). We thank Dan Elhanati for field assistance and helpful discussion during the course of this study. We thank Jan Černý and an anonymous reviewer for providing constructive and very helpful reviews. All the data used for this study is accessible by contacting the authors at ranissachar@gmail.com and is available online at https://figshare.com/articles/Deformation_of_intra-salt_beds_recorded_by_magnetic_fabrics/10247585https://figshare.com.

References

Agnon, A., Weinberger, R., Zak, I., & Sneh, A. (2006). Geological Map of Israel, Sheet 20-I Sedom, scale 1: 50,000. *Geological Survey of Israel, Jerusallem*.

Alsop, G. I., Holdsworth, R. E., & McCaffrey, K. J. W. (2007). Scale invariant sheath folds in salt, sediments and shear zones. *Journal of Structural Geology*, *29*, 1585–1604. https://doi.org/10.1016/J.JSG.2007.07.012

Alsop, G. I., Weinberger, R., Levi, T., & Marco, S. (2015). Deformation within an exposed salt wall: Recumbent folding and extrusion of evaporites in the Dead Sea Basin. *Journal of Structural Geology*, *70*, 95–118. https://doi.org/10.1016/J.JSG.2014.11.006

Alsop, G. I., Weinberger, R., Levi, T., & Marco, S. (2016). Cycles of passive versus active diapirism recorded along an exposed salt wall. *Journal of Structural Geology*, *84*, 47–67. https://doi.org/10.1016/j.jsg.2016.01.008

Alsop, G. I., Weinberger, R., Marco, S., & Levi, T. (2018). Fault and fracture patterns around a strike-slip influenced salt wall. *Journal of Structural Geology*, *106*, 103–124. https://doi.org/10.1016/J.JSG.2017.10.010

Al-Zoubi, A., & ten Brink, U. S. (2001). Salt diapirs in the Dead Sea basin and their relationship to Quaternary extensional tectonics. *Marine and Petroleum Geology*, *18*, 779–797. https://doi.org/10.1016/s0264-8172(01)00031-9

Archer, S. G., Alsop, G. I., Hartley, A. J., Grant, N. T., & Hodgkinson, R. (2012). Salt tectonics, sediments and prospectivity: An introduction. *Geological Society, London, Special Publications*, *363*, 1–6. https://doi.org/10.1144/SP363.1

Aubourg, C., Smith, B., Bakhtari, H., Guya, N., Eshragi, A., Lallemant, S., et al. (2004). Post-Miocene shortening pictured by magnetic fabric across the Zagros-Makran syntaxis (Iran). In *Special Paper 383: Orogenic curvature: Integrating paleomagnetic and structural analyses* (pp. 17–40). https://doi.org/10.1130/0-8137-2383-3(2004)383[17:PSPBMF]2.0.CO;2

Bennett, R. H., Bryant, W. R., & Keller, G. H. (1981). Clay fabric of selected submarine sediments: Fundamental properties and models. *SEPM Journal of Sedimentary Research*, *51*, 217–232. https://doi.org/10.1306/212F7C52-2B24-11D7-8648000102C1865D

Borchert, T. H., & Muir, R. O. (1964). Salt deposits: The origin, metamorphism, and deformation of evaporites. In V. Nostrand (Ed.), *Statistics of earth science data: Their distribution in time, space and orientation*. New York: Statistics of earth science data: their distribution in time, space and orientation.

Borradaile, G. J. (2013). Statistics of earth science data: Their distribution in time, space and orientation. Springer Science & Business Media.

Borradaile, G. J., & Henry, B. (1997). Tectonic applications of magnetic susceptibility and its anisotropy. *Earth-Science Reviews*, *42*, 49–93. https://doi.org/10.1016/s0012-8252(96)00044-x

Borradaile, G. J., & Jackson, M. (2010). Structural geology, petrofabrics and magnetic fabrics (AMS, AARM, AIRM). *Journal of Structural Geology*, *32*, 1519–1551. https://doi.org/10.1016/j.jsg.2009.09.006

Borradaile, G. J., & Tarling, D. H. (1981). The influence of deformation mechanisms on magnetic fabrics in weakly deformed rocks. *Tectonophysics*, *77*, 151–168. https://doi.org/10.1016/0040-1951(81)90165-7

Borradaile, G. J., & Werner, T. (1994). Magnetic anisotropy of some phyllosilicates. *Tectonophysics*, *235*, 223–248. https://doi.org/10.1016/0040-1951(94)90196-1

Burliga, S. (2014). Heterogeneity of folding in Zechstein (Upper Permian) salt deposits in the Kłodawa Salt Structure, central Poland. *Geological Quarterly*. https://doi.org/10.7306/gq.1153

Burliga, S. (2018). Deformation of sediments with salt and shale layers in marginal parts of a basin—A natural example from Miocene deposits in Wieliczka region, Poland. In *20th EGU General Assembly, EGU2018, Proceedings from the conference held 4-13 April, 2018 in Vienna, Austria* (Vol. 20, p. 12213).

Chadima, M., Hansen, A., Hirt, A. M., Hrouda, F., & Siemes, H. (2004). Phyllosilicate preferred orientation as a control of magnetic fabric: Evidence from neutron texture goniometry and low and high-field magnetic anisotropy (SE Rhenohercynian Zone of Bohemian Massif). *Geological Society, London, Special Publications*, *238*, 361–380. https://doi.org/10.1144/GSL.SP.2004.238.01.19

Chemia, Z., & Koyi, H. (2008). The control of salt supply on entrainment of an anhydrite layer within a salt diapir. *Journal of Structural Geology*, *30*, 1192–1200. https://doi.org/10.1016/J.JSG.2008.06.004

Cifelli, F., Mattei, M., & Chadima, M. (2005). The origin of tectonic lineation in extensional basins: Combined neutron texture and magnetic analyses on "undeformed" clays. *Earth and Planetary Science Letters*, *235*, 62–78. http://www.sciencedirect.com/science/article/pii/S0012821X05001871.

Davison, I., Alsop, I., & Blundell, D. (1996). Salt tectonics: some aspects of deformation mechanics. *Special Publication of the Geological Society of London*, *100*, 1–10. https://doi.org/10.1144/GSL.SP.1996.100.01.01

Davison, I., Bosence, D. W. J., Alsop, G. I., & Al-Aawah, M. H. (1996). Deformation and sedimentation around exhumed Miocene salt diapirs, Al-Salif and Jabal al Milh, NW Yemen. *Special Publication of the Geological Society of London*, *100*, 23–39. https://doi.org/10.1144/gsl.sp.1996.100.01.03

Dooley, T. P., Jackson, M. P. A., Jackson, C. A. L., Hudec, M. R., & Rodriguez, C. R. (2015). Enigmatic structures within salt walls of the Santos Basin—Part 2: Mechanical explanation from physical modelling. *Journal of Structural Geology*, *75*, 163–187. https://doi.org/10.1016/J.JSG.2015.01.009

Ebert, Y., Shaar, R., Emmanuel, S., Nowaczyk, N., & Stein, M. (2018). Overwriting of sedimentary magnetism by bacterially mediated mineral alteration. *Geology*, *46*, 291–294. https://doi.org/10.1130/G39706.1

Eyal, Y., & Reches, Z. (1983). Tectonic analysis of the Dead Sea rift region since the Late-Cretaceous based on mesostructures. *Tectonics*, *2*, 39–66. https://doi.org/10.1029/tc002i002p00167

Fiduk, J. C., & Rowan, M. G. (2012). Analysis of folding and deformation within layered evaporites in Blocks BM-S-8 & -9, Santos Basin, Brazil. *Geological Society, London, Special Publications*, *363*, 471–487. https://doi.org/10.1144/SP363.22

Fossen, H. (2016). *Structural geology*. Cambridge University Press.

Frumkin, A. (1996). Structure of northern Mount Sedom salt diapir (Israel) from cave evidence and surface morphology. *Israel Journal of Earth Sciences*, *45*, 73–80.

Gardosh, M., Kashai, E., Salhov, S., & Shulman, H. (1997). Hydrocarbon exploration in the southern Dead Sea area. In T. M. Niemi, Z. Ben-Avraham, & J. R. Gat (Eds.), *The Dead Sea: The lake and its setting*. Oxford monographs on geology and geophysics.

Garfunkel, Z. (1981). Internal structure of the Dead Sea leaky transform (rift) in relation to plate kinematics. *Tectonophysics*, *80*, 81–108. https://doi.org/10.1016/0040-1951(81)90143-8

Garfunkel, Z. (2014). Lateral motion and deformation along the Dead Sea Transform. In *Dead Sea transform fault system: Reviews* (Vol. 6, pp. 109–145). Dordrecht: Springer. https://doi.org/10.1007/978-94-017-8872-4

Graham, R., Jackson, M., Pilcher, R., & Kilsdonk, B. (2012). Allochthonous salt in the sub-Alpine fold–thrust belt of Haute Provence, France. *Geological Society, London, Special Publications*, *363*, 595–615. https://doi.org/10.1144/SP363.30

Hrouda, F., Schulmann, K., Suppes, M., Ullemayer, K., de Wall, H., & Weber, K. (1997). Quantitive relationship between low-field AMS and phyllosilicate fabric: A review. *Physics and Chemistry of the Earth*, *22*, 153–156. https://doi.org/10.1016/S0079-1946(97)00094-3

Issachar, R., Levi, T., Lyakhovsky, V., Marco, S., & Weinberger, R. (2016). Improving the method of low-temperature anisotropy of magnetic susceptibility (LT-AMS) measurements in air. *Geochemistry, Geophysics, Geosystems*, *17*, 2940–2950. https://doi.org/10.1002/2016GC006339

Issachar, R., Levi, T., Marco, S., & Weinberger, R. (2018). Separation of diamagnetic and paramagnetic fabrics reveals strain directions in carbonate rocks. *Journal of Geophysical Research, Solid Earth*, *123*, 2035–2048. https://doi.org/10.1002/2017JB014823

Issachar, R., Levi, T., Marco, S., & Weinberger, R. (2019). Strain field associated with a component of divergent motion along the Southern Dead Sea Fault: Insights from magnetic fabrics. *Tectonics*, 1–19. https://doi.org/10.1029/2018TC005168

Jackson, C. A. L., Jackson, M. P. A., Hudec, M. R., & Rodriguez, C. (2014). Internal structure, kinematics, and growth of a salt wall: Insights from 3-D seismic data. *Geology*, *42*, 307–310. https://doi.org/10.1130/G34865.1

Jackson, M. (1991). Anisotropy of magnetic remanence: A brief review of mineralogical sources, physical origins, and geological applications, and comparison with susceptibility anisotropy. *Pure and Applied Geophysics*, *136*, 1–28. https://doi.org/10.1007/bf00878885

Jackson, M. P. A., & Hudec, M. R. (2017). *Salt tectonics: Principles and practice*. Cambridge University Press.

Jelinek, V. (1981). Characterization of the magnetic fabric of rocks. *Tectonophysics*, *79*, T63–T67. https://doi.org/10.1016/0040-1951(81)90110-4

Kashai, E. L., & Crocker, P. F. (1987). Structural geometry and evolution of the Dead Sea-Jordan rift system as deduced from new subsurface data. *Tectonophysics*, *141*, 33–60. https://doi.org/10.1016/0040-1951(87)90173-9

Koyi, H. A. (2001). Modeling the influence of sinking anhydrite blocks on salt diapirs targeted for hazardous waste disposal. *Geology*, *29*, 387. https://doi.org/10.1130/0091-7613(2001)029<0387:MTIOSA>2.0.CO;2

Larsen, B. D., Ben-Avraham, Z., & Shulman, H. (2002). Fault and salt tectonics in the southern Dead Sea basin. *Tectonophysics*, *346*, 71–90. https://doi.org/10.1016/s0040-1951(01)00229-3

Levi, T., Weinberger, R., Alsop, G. I., & Marco, S. (2018). Characterizing seismites with anisotropy of magnetic susceptibility. *Geology*, *46*, 827–830. https://doi.org/10.1130/G45120.1

Li, S. (2016). A sensitivity study on the numerical model of displacement and deformation of embedded brittle rock bodies in extension environment during salt tectonics. *Arabian Journal of Geosciences*, *9*, 680. https://doi.org/10.1007/s12517-016-2700-7

Li, S., Abe, S., Reuning, L., Becker, S., Urai, J. L., & Kukla, P. A. (2012). Numerical modelling of the displacement and deformation of embedded rock bodies during salt tectonics: A case study from the South Oman Salt Basin. *Geological Society, London, Special Publications*, *363*, 503–520. https://doi.org/10.1144/SP363.24

Maltman, A. J., & Bolton, A. (2003). How sediments become mobilized. *Geological Society, London, Special Publications*, *216*, 9–20. https://doi.org/10.1144/GSL.SP.2003.216.01.02

Milliken, K. L., & Reed, R. M. (2010). Multiple causes of diagenetic fabric anisotropy in weakly consolidated mud, Nankai accretionary prism, IODP Expedition 316. *Journal of Structural Geology*, *32*, 1887–1898. https://doi.org/10.1016/J.JSG.2010.03.008

Oertel, G. (1983). The relationship of strain and preferred orientation of phyllosilicate grains in rocks-a review. *Tectonophysics*, *100*, 413–447. https://doi.org/10.1016/0040-1951(83)90197-X

Parés, J. M. (2015). Sixty years of anisotropy of magnetic susceptibility in deformed sedimentary rocks. *Frontiers in Earth Science*, 3. https://doi.org/10.3389/feart.2015.00004

Parés, J. M., & van der Pluijm, B. A. (2002a). Evaluating magnetic lineations (AMS) in deformed rocks. *Tectonophysics*, *350*, 283–298. https://doi.org/10.1016/S0040-1951(02)00119-1

Parés, J. M., & van der Pluijm, B. A. (2002b). Phyllosilicate fabric characterization by Low-Temperature Anisotropy of Magnetic Susceptibility (LT-AMS). *Geophysical Research Letters*, *29*, 2215. https://doi.org/10.1029/2002GL015459

Parés, J. M., van der Pluijm, B. A., & Dinares-Turell, J. (1999). Evolution of magnetic fabrics during incipient deformation of mudrocks (Pyrenees, northern Spain). *Tectonophysics*, *307*, 1–14. https://doi.org/10.1016/s0040-1951(99)00115-8

Rochette, P. (1988). Inverse magnetic fabric in carbonate-bearing rocks. *Earth and Planetary Science Letters*, *90*, 229–237. https://doi.org/10.1016/0012-821x(88)90103-3

Rowan, M. G., Urai, J. L., Fiduk, J. C., & Kukla, P. A. (2019). Deformation of intrasalt competent layers in different modes of salt tectonics. *Solid Earth Discussions* in review. https://doi.org/10.5194/se-2019-49

Sagy, A., Reches, Z., & Agnon, A. (2003). Hierarchic three-dimensional structure and slip partitioning in the western Dead Sea pull-apart. *Tectonics*, 22. https://doi.org/10.1029/2001tc001323

Sans, M., Sánchez, A. L., & Santanach, P. (1996). Internal structure of a detachment horizon in the most external part of the Pyrenean fold and thrust belt (northern Spain). *Geological Society, London, Special Publications*, *100*, 65–76. https://doi.org/10.1144/GSL.SP.1996.100.01.06

Santolaria, P., Casas, A. M., & Soto, R. (2015). Anisotropy of magnetic susceptibility as a proxy to assess internal deformation in diapirs: Case study of the Naval salt wall (Southern Pyrenees). *Geophysical Journal International*, *202*, 1207–1222. https://doi.org/10.1093/gji/ggv231

Smit, J., Brun, J. P., Fort, X., Cloetingh, S., & Ben-Avraham, Z. (2008). Salt tectonics in pull-apart basins with application to the Dead Sea Basin. *Tectonophysics*, *449*, 1–16. https://doi.org/10.1016/j.tecto.2007.12.004

Sneh, A., and Weinberger, R., 2014, *Major structures of Israel and Environs, scale 1: 500,000*: Geological Survey of Israel, Jerusalem.

Soto, R., Beamud, E., Oliva-Urcia, B., & Roca, E. (2014). Applicability of magnetic fabrics in rocks associated with the emplacement of salt structures (the Bicorb–Quesa and Navarrés salt walls, Prebetics, SE Spain). *Tectonophysics*, *629*, 319–334. https://doi.org/10.1016/j.tecto.2014.07.004

Strozyk, F., Van Gent, H., Urai, J. L., & Kukla, P. A. (2012). 3D seismic study of complex intra-salt deformation: An example from the Upper Permian Zechstein 3 stringer, western Dutch offshore. *Geological Society, London, Special Publications*, *363*, 489–501. https://doi.org/10.1144/SP363.23

Talbot, C. J. (1998). Extrusions of Hormuz salt in Iran. *Geological Society, London, Special Publications*, *143*, 315–334. https://doi.org/10.1144/gsl.sp.1998.143.01.21

Tarling, D. H., & Hrouda, F. H. (1993). *The magnetic anisotropy of rocks: London*. Chapman and Hall, 217 p., http://www.google.co.il/books?hl=en&lr=&id=Y90eoA8llY4C&pgis=1.

Urai, J., Schléder, Z., & Spiers, C. (2008). Flow and transport properties of salt rocks. In *Dynamics of complex intracontinental basins: The central European basin system* (pp. 277–290). Springer Science & Business Media.

van der Pluijm, B. A., & Kaars-Sijpesteijn, C. H. (1984). Chlorite-mica aggregates: Morphology, orientation, development and bearing on cleavage formation in very-low-grade rocks. *Journal of Structural Geology*, *6*, 399–407. https://doi.org/10.1016/0191-8141(84)90040-3

Van Gent, H., Urai, J. L., & de Keijzer, M. (2011). The internal geometry of salt structures—A first look using 3D seismic data from the Zechstein of the Netherlands. *Journal of Structural Geology*, *33*, 292–311. https://doi.org/10.1016/J.JSG.2010.07.005

Warren, J. K. (2016). *Evaporites: A geological compendium: Berlin*. Germany: Springer.

Warren, J. K. (2017). Salt usually seals, but sometimes leaks: Implications for mine and cavern stabilities in the short and long term. *Earth-Science Reviews*, *165*, 302–341. https://doi.org/10.1016/J.EARSCIREV.2016.11.008

Weinberger, R., Agnon, A., & Ron, H. (1997). Paleomagnetic reconstruction of a diapir emplcement: A case study from Sedom diapir, the Dead Sea Rift. *Journal of Geophysical Research*, *102*(p), 5173–5192. https://doi.org/10.1029/96jb02287

Weinberger, R., Agnon, A., Ron, H., & Garfunkel, Z. (1995). Rotation about an inclined axis: Three dimensional matrices for reconstructing paleomagnetic and structural data. *Journal of Structural Geology*, *17*, 777–782. https://doi.org/10.1016/0191-8141(94)00108-c

Weinberger, R., Bar-Matthews, M., Levi, T., & Begin, Z. B. (2007). Late-Pleistocene rise of the Sedom diapir on the backdrop of water-level fluctuations of Lake Lisan, Dead Sea basin. *Quaternary International*, *175*, 53–61. https://doi.org/10.1016/J.QUAINT.2007.03.007

Weinberger, R., Begin, Z. B., Waldmann, N., Gardosh, M., Baer, G., Frumkin, A., & Wdowinski, S. (2006). Quaternary rise of the Sedom diapir, Dead Sea basin. In *Special Paper 401: New Frontiers in Dead Sea Paleoenvironmental Research* (pp. 33–51). Geological Society of America. https://doi.org/10.1130/2006.2401(03)

Weinberger, R., Levi, T., Alsop, G. I., & Marco, S. (2017). Kinematics of mass transport deposits revealed by magnetic fabrics. *Geophysical Research Letters*, *44*, 7743–7749. https://doi.org/10.1002/2017GL074471

Weinberger, R., Lyakhovsky, V., Baer, G., & Begin, Z. B. (2006). Mechanical modeling and InSAR measurements of Mount Sedom uplift, Dead Sea basin: Implications for effective viscosity of rock salt. *Geochemistry, Geophysics, Geosystems*, *7*. https://doi.org/10.1029/2005gc001185

Zak, I. (1967). *The geology of Mount Sedom [Ph.D. thesis]*. Hebrew University. 208 p.

Zak, I., & Freund, R. (1980). Strain measurements in eastren marginal shear zone of Mount Sedom salt diapir. *AAPGBulletin*, *64*, 568–581. https://doi.org/10.1306/2f918a7c-16ce-11d7-8645000102c1865d

Zak, I., Karcz, I., & Key, C. A. (1968). Significance of some sedimentary structures from Mount Sedom. *Israel Journal of Earth Sciences*, *17*, 1.

Zucker, E., Frumkin, A., Agnon, A., & Weinberger, R. (2019). Internal deformation and uplift-rate of salt walls detected by a displaced dissolution surface, Dead Sea basin. *Journal of Structural Geology*, *127*, 103870. https://doi.org/10.1016/J.JSG.2019.103870